# Imaging of High-Speed Aerial Targets With ISAR Installed on a Moving Vessel

Dau-Ming Wu and Jean-Fu Kiang, *Life Senior Member, IEEE*

***Abstract*—An inverse synthetic aperture radar (ISAR) technique is proposed to acquire high-resolution steady images of high-speed aerial target with radar installed on a moving vessel. The phase changes due to target motion and attitude perturbation of the vessel are compensated. A 2-D ISAR imaging method is enhanced to acquire 3-D-compatible images of uncooperative targets. The target motion parameters are fine-tuned iteratively to better focus the target image. A $(\zeta_h, \zeta_v)$ plane is proposed to display 3-D targets for visual-like perception. The 2-D ISAR images, thus, focused on the preserve features of the original 3-D targets, including shape and size. Imaging of several aerial targets is simulated to demonstrate the efficacy of the proposed approach.**

***Index Terms*—Attitude perturbation, inverse synthetic aperture radar (ISAR), iterative focusing, visual-like perception.**

## I. Introduction

INVERSE synthetic aperture radar (ISAR) techniques [1] have been widely used to acquire images of aircrafts [2], [3], maritime vessels [4], [5], and space targets [6], [7], by exploiting the relative motion between target and radar platform during an aperture time. The 3-D motion of a target is typically mapped to a 2-D image project plane (IPP). The motion parameters of a target are needed to derive an azimuth scale for estimating the target size [8].

A high-speed and highly maneuvering target yields a complicated range model within the aperture time. In [9], an entropy-based ISAR image autofocusing approach was proposed to acquire well-focused images of highly maneuvering targets. In [10], a coherent integrated smoothed generalized cubic phase function was proposed to acquire well-focused ISAR image of a space target. In [11], an ISAR imaging method on an aerial target with low signal-to-noise ratio (SNR) was proposed, by combining a multidelay discrete polynomial-phase transform and keystone transform.

Typical ISAR systems, including bistatic [12] and multistatic [6] variants, are assumed to operate on a stationary platform for surveillance of moving targets. ISAR imaging was also conducted on moving platforms, such as ship, satellite [13], or aerostat [14], for the sake of mobility and flexibility, under the challenges of nonstationary IPP and line of sight. A platform under perturbed motion induces additional phase error to the backscattered signals [14], [15], imposing more challenges on conventional ISAR imaging methods [13]. In [13], a satellite-borne ISAR imaging approach on moving ship was proposed. A nonstationary IPP was derived and a particle swarm optimization algorithm was applied for compensating the 2-D spatial phase error to acquire a well-focused ISAR image.

Computational electromagnetic models have been used to simulate the backscattered signals from an aerial target, which is more convenient and flexible than measuring real radar echoes [16]. In [17], a computer-aided design model of a target was built, and its surface was approximated as perfect electric conductor. The backscattered signals from the target were computed by using a shooting-and-bouncing ray technique. In [16], an interferometric ISAR (InISAR) approach was proposed, with a target ship modeled as 3-D point cloud.

3-D ISAR images can be acquired with techniques of sequential ISAR [18], InISAR, and polarimetric InISAR [19]. A 3-D high-resolution ISAR image is typically reconstructed from a sequence of 2-D ISAR images on the same target acquired in monostatic configuration [5], [18]. Conventional interferometric techniques require at least three radar antennas to form two orthogonal baselines [5], and the 3-D target information is retrieved from the interference term.

In [20], a 3-D InISAR imaging method based on range-Doppler algorithm was proposed. Instead of processing the interference term between baselines, specific peaks in a series of defocused images were used to construct a high-resolution 3-D image at reduced computational cost. In [21], a radar system model for 3-D InISAR imaging was proposed, relaxing the constraint that the two baselines be strictly orthogonal.

Compared with ISAR system of single polarization, polarimetric InISAR can be used to extract more precise geometry of targets [22]. In [19], a 3-D polarimetric InISAR imaging method on noncooperative target was proposed, with three fully polarized radars forming two orthogonal baselines. The 2-D ISAR images acquired at three radars were coregistered and a coherent optimization approach was applied to extract relevant 3-D information.

In this work, an ISAR imaging method on high-speed aerial target is proposed, with one active radar and one passive receiver installed on a moving vessel bearing attitude perturbation [23]. However, most 3-D ISAR imaging approaches were based on static radar platform, which cannot be applied to a moving platform without modifications. Hence, a 2-D ISAR imaging configuration is adopted in this work, and an iterative

Manuscript received 7 April 2023; revised 10 June 2023; accepted 5 July 2023. Date of publication 11 July 2023; date of current version 21 July 2023. *(Corresponding author: Jean-Fu Kiang.)*

The authors are with the Graduate Institute of Communication Engineering, National Taiwan University, Taipei 10617, Taiwan (e-mail: r07942105@ntu.edu.tw; jfkiang@ntu.edu.tw, jfkiang@cc.ee.ntu.edu.tw).

Digital Object Identifier 10.1109/JSTARS.2023.3294135

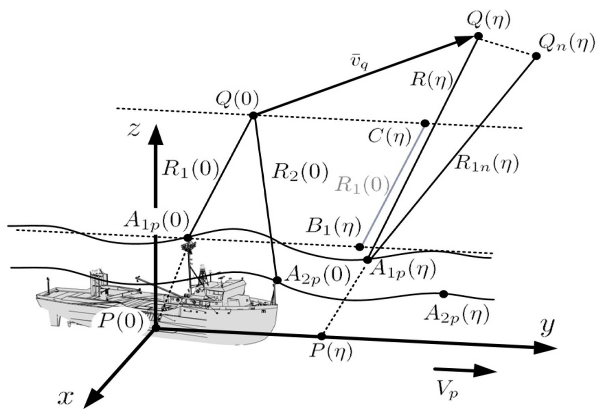


Fig. 1. Schematic of ISAR imaging on aerial target centered at $Q(\eta)$, vessel centered at $P(\eta)$ moves in $y$ direction at constant speed $V_p$, and radar antennas are located at $A_{1p}(\eta)$ and $A_{2p}(\eta)$, respectively.

coordinate estimation procedure is developed to reconstruct a faithful visual-like image, which can be augmented with range information to form a holograph-like 3-D image. A 3-D ISAR imaging approach based on moving platforms will be developed on top of this technique later.

In this work, physical optics (PO) approximation is used to simulate the backscattered signals from the target [16]. The phase error induced by vessel attitude perturbation is approximated as a polynomial of slow time. A range-frequency reversal transform (RFRT) and a fractional Fourier transform (FrFT) are applied to estimate the target motion parameters, which are then used to compensate for the phase error attributed to target motion. An iterative procedure is developed to update the target velocity vector, correct the image distortion, adjust the cross-range scaling, and fine-tune the target position.

The rest of this article is organized as follows. The range model incorporating target motion and vessel attitude perturbation is presented in Section II. The method to compensate the phase error induced by attitude perturbation is presented in Section III. Motion compensation and imaging of the target are presented in Section IV. Image quality and target recognition are demonstrated and discussed in Section V. Finally, Section VI concludes this article.

## II. Range Model

Fig. 1 shows the schematic of ISAR imaging on an aerial target centered at $Q(\eta)$, with radars located at $A_{1p}(\eta)$ and $A_{2p}(\eta)$, respectively, on a vessel. The vessel is centered at $P(\eta)$ and moves in $y$ direction at a constant speed $V_p$. The target is modeled as a collection of $N_q$ scatterers, $\{Q_n(\eta)\}$, around the target center $Q(\eta)$. During the aperture time interval, the position of the target center is given by

$$Q(\eta) = Q(0) + \bar{v}_q\eta$$

where $Q(0) = (x_q, y_q, z_q)$ is the target position at $\eta = 0$, with

$$x_q = R_s(0)\cos\theta_{se}\cos\phi_{sa}$$
$$y_q = R_s(0)\cos\theta_{se}\sin\phi_{sa}$$
$$z_q = R_s(0)\sin\theta_{se}$$

where $R_s(0)$ is the slant range at $\eta = 0$, $\phi_{sa}$ and $\theta_{se}$ are the azimuth and elevation angles, respectively, measured from antenna $s$, and $\bar{v}_q = [v_x, v_y, v_z]^t$ is the target velocity vector. The position of the vessel center is given by

$$P(\eta) = \bar{V}_p\eta = (0, V_p\eta, 0)$$

where $\bar{V}_p = [0, V_p, 0]^t$ is the platform velocity.

The attitude perturbation of the vessel is characterized with $\bar{\bar{\Omega}}_a(\eta)$, the product of three rotational matrices specified by yaw $\theta_y(\eta)$, pitch $\theta_p(\eta)$, and roll $\theta_r(\eta)$, respectively. Explicitly, the position of antenna $s$ is given by

$$A_{sp}(\eta) = P(\eta) + \bar{w}_s(\eta) = \bar{V}_p\eta + \bar{\bar{\Omega}}_a(\eta)\cdot\bar{w}_s(0)$$

where $\bar{w}_s(\eta)$ is the displacement of antenna $s$ with respect to the vessel center.

Let us define the reference points $B_s(\eta)$ and $C(\eta)$ by laterally shifting antenna $s$ and the target at $\eta = 0$, respectively, with an amount $\bar{V}_p\eta$, namely

$$\begin{aligned} B_s(\eta) &= A_{sp}(0) + \bar{V}_p\eta = \bar{\bar{\Omega}}_a(0)\cdot\bar{w}_s(0) + \bar{V}_p\eta \\ C(\eta) &= Q(0) + \bar{V}_p\eta. \end{aligned}$$

Since $\overline{B_s(\eta)C(\eta)}$ is independent of $\eta$, it is relabeled as $\overline{B_sC}$, with length of $R_s(0) = |\overline{B_sC}| = |Q(0) - \bar{\bar{\Omega}}_a(0)\cdot\bar{w}_s(0)|$. As shown in Fig. 1, the range difference due to the translational motion of the target is approximated as

$$\Delta R_{st} = \left|\overline{B_s(\eta)Q(\eta)}\right| - \left|\overline{B_sC}\right| \simeq \alpha_{s1}\eta + \alpha_{s2}\eta^2. \quad (1)$$

Similarly, the range difference due to the attitude perturbation of platform is approximated as

$$\Delta R_{sa} = \left|\overline{A_{sp}(\eta)C(\eta)}\right| - \left|\overline{B_sC}\right| \simeq \beta_{s1}\eta + \beta_{s2}\eta^2 + \beta_{s3}\eta^3.$$

The range between antenna $s$ at $A_{sp}(\eta)$ and the target center at $Q(\eta)$ is thus approximated as

$$\begin{aligned} R_s(\eta) &= \left|\overline{A_{sp}(\eta)Q(\eta)}\right| \simeq \left|\overline{B_sC}\right| + \Delta R_{st} + \Delta R_{sa} \\ &\simeq R_s(0) + (\alpha_{s1}+\beta_{s1})\eta + (\alpha_{s2}+\beta_{s2})\eta^2 + \beta_{s3}\eta^3. \end{aligned}$$

The position of the $n$th scatterer at $\eta$ is given by

$$Q_n(\eta) = Q(\eta) + \bar{r}_n$$

where $\bar{r}_n = (x_n, y_n, z_n)$ is its relative position about the target center. The range between antenna $s$ and the $n$th scatterer is computed as

$$\begin{aligned} R_{sn}(\eta) &= \left|\overline{A_{sp}(\eta)Q_n(\eta)}\right| = \left|\overline{A_{sp}(\eta)Q(\eta)} + \bar{r}_n\right| \\ &\simeq \left|\overline{A_{sp}(\eta)Q(\eta)}\right| + \bar{r}_n\cdot\overline{B_s(\eta)Q(\eta)}/\left|\overline{B_s(\eta)Q(\eta)}\right| \\ &\simeq R_s(0) + \bar{r}_n\cdot\left(\hat{b}_s + \frac{\bar{v}_q - \bar{V}_p}{R_s(0)}\right)\eta \\ &\quad + (\alpha_{s1}+\beta_{s1})\eta + (\alpha_{s2}+\beta_{s2})\eta^2 + \beta_{s3}\eta^3 \end{aligned} \quad (2)$$

where $|\overline{B_s(\eta)Q(\eta)}| \simeq |\overline{B_sC}| + \hat{b}_s\cdot(\bar{v}_q - \bar{V}_p)\eta \simeq R_s(0)$, and $\hat{b}_s$ is the unit vector of $\overline{B_sC}$.

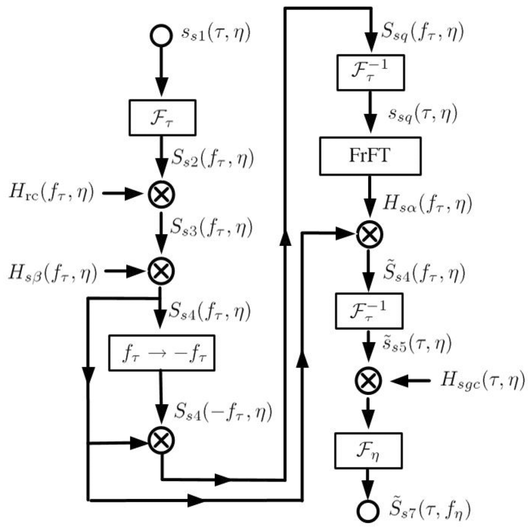


Fig. 2. Flowchart of proposed ISAR imaging approach.

TABLE I
RADAR PARAMETERS USED IN SIMULATIONS

| parameter | symbol | value | ref. |
|---|---|---|---|
| carrier frequency | $f_c$ | 10 GHz | [24] |
| chirp pulse duration | $T_r$ | 10 $\mu$s | [25] |
| range chirp rate | $K_r$ | 100 THz/s | |
| bandwidth | $B_r$ | 1,000 MHz | [26] |
| range sampling rate | $F_r$ | 1,200 MHz | |
| number of range samples | $N_r$ | 2,048 | |
| pulse repetition frequency | $F_a$ | 512 Hz | [24] |
| number of azimuth samples | $N_a$ | 512 | |
| platform velocity | $V_p$ | 16 m/s | |
| position of antenna 1 | $\bar{w}_1(0)$ | $[0,0,23.46]^t$ m | |
| position of antenna 2 | $\bar{w}_2(0)$ | $[0,-100,20]^t$ m | |

## III. Compensation of Attitude Perturbation

Fig. 2 shows the flowchart of the proposed ISAR imaging approach, and Table I lists the radar parameters used in the simulations. A linear frequency modulation pulse

$$s_0(\tau) = \mathrm{rect}(\tau/T_r)e^{j2\pi f_c\tau}e^{j\pi K_r\tau^2}$$

is periodically radiated toward the target, where $\tau$ is the fast time, $K_r$ is the chirp rate, $T_r$ is the pulse width, and $\mathrm{rect}(t)$ is a window function, which is one if $|t| \le 1/2$ and zero, otherwise. The backscattered signal from the moving target is received at antenna $s$ and demodulated as

$$s_{s1}(\tau,\eta) = \mathrm{rect}\left(\eta/T_a\right)\sum_{n=1}^{N_q} A_{sn}\mathrm{rect}\left(\frac{\tau-\tau_{sn}}{T_r}\right)$$
$$e^{-j4\pi f_c R_{sn}(\eta)/c}e^{j\pi K_r(\tau-\tau_{sn})^2}$$

where $\eta$ is the slow time, and $A_{sn}$ is the amplitude of backscattered signal from the $n$th scatterer, which is received with time delay $\tau_{sn} = 2R_{sn}(\eta)/c$.

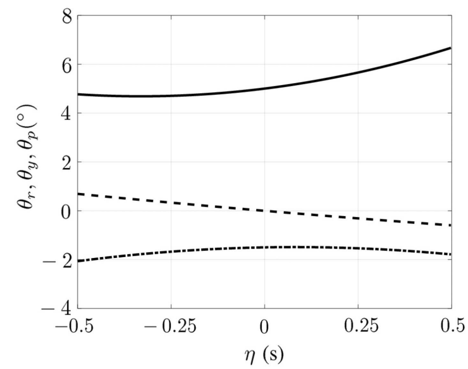


Fig. 3. Attitude data of a moving vessel [23]. ———: roll angle ($\theta_r$). − − −: yaw angle ($\theta_y$). − · −: pitch angle ($\theta_p$).

The received signal is range compressed by first taking the range Fourier transform of $s_{s1}(\tau,\eta)$ to have

$$S_{s2}(f_\tau,\eta) = \mathcal{F}_\tau\left\{s_{s1}(\tau,\eta)\right\} = \mathrm{rect}\left(\eta/T_a\right)\sum_{n=1}^{N_q} A_{sn}$$
$$\mathrm{rect}\left(f_\tau/B_r\right)e^{-j\pi f_\tau^2/K_r}e^{-j4\pi(f_c+f_\tau)R_{sn}(\eta)/c}$$

which is multiplied with a range compression filter $H_{\rm rc}(f_\tau,\eta) = e^{j\pi f_\tau^2/K_r}$ to have

$$\begin{aligned} S_{s3}(f_\tau,\eta) &= S_{s2}(f_\tau,\eta)H_{\rm rc}(f_\tau,\eta) \\ &= \mathrm{rect}\left(\eta/T_a\right)\sum_{n=1}^{N_q} A_{sn}\mathrm{rect}\left(f_\tau/B_r\right) \\ &\quad\times e^{-j4\pi(f_c+f_\tau)\chi_{sn}(\eta)/c} \\ &\quad e^-j4\pi(f_c+f_\tau)[R_s(0)+(\alpha_{s1}+\beta_{s1})\eta \\ &\quad+(\alpha_{s2}+\beta_{s2})\eta^2+\beta_{s3}\eta^3]/c \end{aligned} \tag{3}$$

where

$$\chi_{sn}(\eta) = \bar{r}_n \cdot \left(\hat{b}_s + \frac{\bar{v}_q - \bar{V}_p}{R_s(0)}\eta\right). \tag{4}$$

Fig. 3 shows the attitude data (yaw, roll, and pitch) of a moving vessel [23], which are used in the simulations.

## IV. Motion Compensation and Imaging of Target

Typical ISAR methods map the target image on the range-Doppler plane. The range information of target can be retrieved by processing the backscattered signals. However, to focus the image of a target with translational motion, the target velocity components ($v_x$ and $v_y$) are needed to compensate for geometrical distortion and conduct Doppler–azimuth scaling. Moreover, since the target velocity $(v_x, v_y)$ and position $(x_q, y_q)$ are intertwined in the phase of received signals, the target position at a reference slow time ($\eta = 0$) is needed to attain accurate velocity estimation.

Let us assume that the target at $\eta = 0$ is located at $(\phi_{sa}^{(0)}, \theta_{se}^{(0)})$, with confidence interval of $(-0.1^\circ, 0.1^\circ)$, at SNR $= 5$ dB [27]. The unit vectors in range and cross-range directions with respect to antenna $s$ at $\eta = 0$ can be estimated as

$$\hat{u}_{sr}^{(0)} = [\cos\theta_{se}^{(0)} \cos\phi_{sa}^{(0)}, \cos\theta_{se}^{(0)} \sin\phi_{sa}^{(0)}, \sin\theta_{se}^{(0)}]^t \tag{5}$$

$$\hat{u}_{scr}^{(0)} = [\sin\phi_{sa}^{(0)}, -\cos\phi_{sa}^{(0)}, 0]^t \tag{6}$$

and the target center with respect to antenna $s$ at $\eta = 0$ can be estimated as

$$x_{sq}^{(0)} = R_{s0}^{(0)} \cos\theta_{se}^{(0)} \cos\phi_{sa}^{(0)} \tag{7}$$

$$y_{sq}^{(0)} = R_{s0}^{(0)} \cos\theta_{se}^{(0)} \sin\phi_{sa}^{(0)} \tag{8}$$

$$z_{sq}^{(0)} = R_{s0}^{(0)} \sin\theta_{se}^{(0)} \tag{9}$$

which are averaged over $s = 1, 2$ to determine the target center at $\eta = 0$ as $Q_0^{(0)} = (x_q^{(0)}, y_q^{(0)}, z_q^{(0)})$, with

$$\begin{aligned} x_q^{(0)} &= \frac{1}{2}(x_{1q}^{(0)} + x_{2q}^{(0)}) \\ y_q^{(0)} &= \frac{1}{2}(y_{1q}^{(0)} + y_{2q}^{(0)}) \\ z_q^{(0)} &= \frac{1}{2}(z_{1q}^{(0)} + z_{2q}^{(0)}). \end{aligned} \tag{10}$$

The target position will be fine-tuned by iteration. In the $\ell$th iteration, the target position is updated as $Q_0^{(\ell)} = [x_q^{(\ell)}, y_q^{(\ell)}, z_q^{(\ell)}]^t$, and its distance to radar $s$ is

$$R_{s0}^{(\ell)} = \sqrt{(x_q^{(\ell)} - x_{sa})^2 + (y_q^{(\ell)} - y_{sa})^2 + (z_q^{(\ell)} - z_{sa})^2}.$$

The range difference caused by attitude perturbation of platform is represented as

$$\Delta R_{sa}^{(\ell)}(\eta) = \left|\overline{A_{sp}(\eta) C^{(\ell)}(\eta)}\right| - \left|\overline{B_s C^{(\ell)}(\eta)}\right| \tag{11}$$

where

$$C^{(\ell)}(\eta) = Q_0^{(\ell)} + \bar{V}_p \eta.$$

Since the attitudes of platform and radar $s$ ($A_{sp}(\eta)$) are known, the range difference due to attitude perturbation of platform is represented as a polynomial of $\eta$ as $\Delta R_{sa}^{(\ell)}(\eta) = \beta_{s1}^{(\ell)}\eta + \beta_{s2}^{(\ell)}\eta^2 + \beta_{s3}^{(\ell)}\eta^3$. The coefficients $\beta_{s1}^{(\ell)}$, $\beta_{s2}^{(\ell)}$, and $\beta_{s3}^{(\ell)}$ are estimated by applying regression fit on $\Delta R_{sa}^{(\ell)}(\eta)$ given in (11).

With the estimated coefficients $\beta_{sn}^{(\ell)}$ ($n = 1, 2, 3$), a compensation filter is designed as

$$H_{s\beta}^{(\ell)}(f_\tau, \eta) = e^{j4\pi(f_c + f_\tau)[\beta_{s1}^{(\ell)}\eta + \beta_{s2}^{(\ell)}\eta^2 + \beta_{s3}^{(\ell)}\eta^3]/c}$$

which is multiplied with (3) to have

$$\begin{aligned} S_{s4}^{(\ell)}(f_\tau, \eta) &= S_{s3}(f_\tau, \eta) H_{s\beta}^{(\ell)}(f_\tau, \eta) \\ &\simeq \text{rect}\,(\eta/T_a) \sum_{n=1}^{N_q} A_{sn} \text{rect}\,(f_\tau/B_r) \\ &\quad e^{-j4\pi(f_c+f_\tau)[R_s(0)+\chi_{sn}(\eta)]/c} e^{-} j4\pi(f_c + f_\tau) \\ &\quad (\alpha_{s1}\eta + \alpha_{s2}\eta^2)/c. \end{aligned}$$

Thus, the attitude perturbation of platform can be compensated.

### A. Estimation of Motion Parameters

The range-compressed signals of a high-speed aerial target migrate over many range cells, hence conventional techniques of range alignment and phase adjustment may not work well, especially at low SNR [11]. In this work, an RFRT [28] is applied to compensate the range-cell migration embedded in $S_{s4}^{(\ell)}(f_\tau, \eta)$, squeezing the range-compressed signals into a small number of range cells.

First, reverse the range frequency in $S_{s4}^{(\ell)}(f_\tau, \eta)$ and multiply it with $S_{s4}^{(\ell)}(f_\tau, \eta)$ to have

$$S_{sq}^{(\ell)}(f_\tau, \eta) = S_{s4}^{(\ell)}(f_\tau, \eta) S_{s4}^{(\ell)}(-f_\tau, \eta) = \text{rect}\,(\eta/T_a) \sum_{n=1}^{N_q} A_{sn}^2$$
$$\text{rect}\,(f_\tau/B_r)\, e^{-j8\pi f_c[R_s(0)+\chi_{sn}(\eta)]/c} e^{-j8\pi f_c(\alpha_{s1}\eta + \alpha_{s2}\eta^2)/c}.$$

Then, take the inverse Fourier transform of $S_{sq}^{(\ell)}(f_\tau, \eta)$ in range to have

$$s_{sq}^{(\ell)}(\tau, \eta) = \mathcal{F}_\tau^{-1}\left\{S_{sq}^{(\ell)}(f_\tau, \eta)\right\} = \text{rect}\,(\eta/T_a) \sum_{n=1}^{N_q} A_{sn}^2 B_r$$
$$\text{sinc}\{B_r\tau\} e^{-j8\pi f_c[R_s(0)+\chi_{sn}(\eta)]/c} e^{-j8\pi f_c(\alpha_{s1}\eta + \alpha_{s2}\eta^2)/c}$$

where the translational motion of target is embedded in the last phase term.

Next, take an FrFT of $s_{sq}^{(\ell)}(\tau, \eta)$ to have [28]

$$S_{sq}^{(\ell)}(\tau, \phi, u) = \int_{-\infty}^{\infty} K_\phi(u, \eta) s_{sq}^{(\ell)}(\tau, \eta) d\eta \tag{12}$$

with the kernel

$$K_\phi(u, \eta) = \begin{cases} \sqrt{1 - j\cot\phi}\, e^{j\pi\left(\eta^2\cot\phi - 2u\eta\csc\phi + u^2\cot\phi\right)} \\ \qquad \phi \neq n\pi \\ \delta(u - \eta), \quad \phi = 2n\pi \\ \delta(u + \eta), \quad \phi = (2n \pm 1)\pi. \end{cases}$$

Explicitly, (12) is reduced to t

$$S_{sq}^{(\ell)}(\tau, \phi, u) \simeq \sqrt{1 - j\cot\phi} \sum_{n=1}^{N_q} e^{j\pi u^2 \cot\phi}$$
$$\int_{-T_a/2}^{T_a/2} e^{-j2\pi(\gamma_{s1}\eta + \gamma_{s2}\eta^2)} d\eta \tag{13}$$

with

$$\gamma_{s1} = \frac{4\alpha_{s1}}{\lambda_c} + u\csc\phi \tag{14}$$

$$\gamma_{s2} = \frac{4\alpha_{s2}}{\lambda_c} - 0.5\cot\phi \tag{15}$$

where $\lambda_c = c/f_c$ is the wavelength at the center frequency. If $\gamma_{s2} = 0$, (13) becomes

$$S_{sq}^{(\ell)}(\tau, \phi, u) = \sqrt{1 - j\cot\phi} \sum_{n=1}^{N_q} e^{j\pi u^2 \cot\phi}$$

TABLE II
PARAMETERS OF SIMULATED TARGET

| parameter | symbol | value |
|---|---|---|
| $x$ coordinate | $x_q$ | 6000 m |
| $y$ coordinate | $y_q$ | 3464.1 m |
| $z$ coordinate | $z_q$ | 12000 m |
| velocity in $x$ | $v_x$ | 50 m/s |
| velocity in $y$ | $v_y$ | −300 m/s |
| velocity in $z$ | $v_z$ | 0 m/s |

$$T_a \mathrm{sinc}\left\{T_a\left(u\csc\phi + 4\alpha_{s1}/\lambda_c\right)\right\} \tag{16}$$

where the sinc function indicates a peak value at $(u, \phi) = (u_g, \phi_g)$, leading to

$$\alpha_{s1}^{(\ell)} = -\frac{u_g\lambda_c\csc\phi_g}{4}. \tag{17}$$

By imposing $\gamma_{s2} = 0$ and $\phi = \phi_g$ in (15), we have

$$\alpha_{s2}^{(\ell)} = \frac{\lambda_c\cot\phi_g}{8}. \tag{18}$$

From (1), the coefficients $\alpha_{s1}^{(\ell)}$ and $\alpha_{s2}^{(\ell)}$ are related to the target position and velocity, in the $\ell$th iteration, as

$$\alpha_{s1}^{(\ell)} = \frac{v_x^{(\ell)}(x_q^{(\ell)} - x_{sa}) + (v_y^{(\ell)} - V_p)(y_q^{(\ell)} - y_{sa})}{R_{s0}^{(\ell)}} \tag{19}$$

$$\begin{aligned}\alpha_{s2}^{(\ell)} &= \frac{v_x^{(\ell)2} + (v_y^{(\ell)} - V_p)^2}{2R_{s0}^{(\ell)}} \\ &\quad - \frac{[v_x^{(\ell)}(x_q^{(\ell)} - x_{sa}) + (v_y^{(\ell)} - V_p)(y_q^{(\ell)} - y_{sa})]^2}{2R_{s0}^{(\ell)3}}\end{aligned} \tag{20}$$

where $\bar{w}_s(0) = (x_{sa}, y_{sa}, z_{sa})$ is the displacement of antenna $s$ with respect to the vessel center at $\eta = 0$.

### *B. Velocity Estimation and Fine-Tuning*

The target position can be specified in terms of the propagation delay and the direction-of-arrival $(\theta_{se}^{(\ell)}, \phi_{sa}^{(\ell)})$ of the backscattered signal. Since the target is far away from the radar, a tiny error in the estimated target direction will yield significant offset in the target position, which in turn will yield inaccurate velocity estimation. An iterative procedure is developed to update the velocity first, followed by adjustment of target position and angular direction of the target center. The loop continues until convergence is reached.

Table II lists the parameters of a simulated target. The target velocity $v_{sx}^{(\ell)}$ and $v_{sy}^{(\ell)}$ can be estimated by solving (19) and (20) to have

$$\begin{aligned}v_{sx}^{(\ell)} &= \frac{R_{s0}^{(\ell)}\alpha_{s1}^{(\ell)}[x_q^{(\ell)} - x_{sa}]}{[x_q^{(\ell)} - x_{sa}]^2 + [y_q^{(\ell)} - y_{sa}]^2} \pm \Big\{[y_q^{(\ell)} - y_{sa}]^2[\alpha_{s1}^{(\ell)}]^2 \\ &\quad \times\left([x_q^{(\ell)} - x_{sa}]^2 + [y_q^{(\ell)} - y_{sa}]^2 - [R_{s0}^{(\ell)}]^2\right) + 2R_{s0}^{(\ell)}\alpha_{s2}^{(\ell)} \\ &\quad \times [y_q^{(\ell)} - y_{sa}]^2\left([x_q^{(\ell)} - x_{sa}]^2 + [y_q^{(\ell)} - y_{sa}]^2\right)\Big\}^{1/2}\end{aligned} \tag{21}$$

TABLE III
VELOCITY ESTIMATION ON ± SIGNS

| ± sign | $v_{1x}$ (m/s) | $v_{2x}$ (m/s) | $v_{1y}$ (m/s) | $v_{2y}$ (m/s) |
|---|---|---|---|---|
| $(+,+)$ | 49.99 | 49.99 | 193.4 | 187.6 |
| $(+,-)$ | −234.8 | −239.5 | 193.4 | 187.6 |
| $(-,+)$ | 49.99 | 49.99 | −300.08 | −300.1 |
| $(-,-)$ | −234.8 | −239.5 | −300.08 | −300.1 |

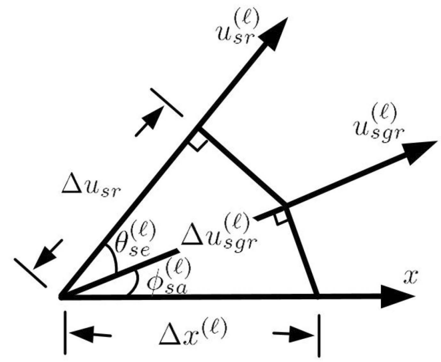


Fig. 4. Geometrical relation between $u_{sr}^{(\ell)}$, $u_{sgr}^{(\ell)}$, and $x$-axes.

$$\begin{aligned}v_{sy}^{(\ell)} &= V_p + \frac{R_{s0}^{(\ell)}\alpha_{s1}^{(\ell)}[y_q^{(\ell)} - y_{sa}]}{[x_q^{(\ell)} - x_{sa}]^2 + [y_q^{(\ell)} - y_{sa}]^2} \pm \Big\{[x_q^{(\ell)} - x_{sa}]^2 \\ &\quad [\alpha_{s1}^{(\ell)}]^2\left([x_q^{(\ell)} - x_{sa}]^2 + [y_q^{(\ell)} - y_{sa}]^2 - [R_{s0}^{(\ell)}]^2\right) \\ &\quad + 2R_{s0}^{(\ell)}\alpha_{s2}^{(\ell)}[x_q^{(\ell)} - x_{sa}]^2 \\ &\quad \times\left([x_q^{(\ell)} - x_{sa}]^2 + [y_q^{(\ell)} - y_{sa}]^2\right)\Big\}^{1/2} \\ &\quad \times\left([x_q^{(\ell)} - x_{sa}]^2 + [y_q^{(\ell)} - y_{sa}]^2\right)^{-1}\end{aligned} \tag{22}$$

where the ambiguity created by the ± sign can be eliminated by crossreferencing the estimated velocities from both radars $s = 1, 2$. Table III shows that picking - sign for $s = 1$ and + sign for $s = 2$ yields consistent $v_{sx}^{(\ell)}$ and $v_{sy}^{(\ell)}$, which are also close to the true values. It is observed by simulations that picking wrong sign for $v_{sx}^{(\ell)}$ distorts the acquired image in range direction, and picking wrong sign for $v_{sy}^{(\ell)}$ reverses the moving direction of the target in azimuth direction.

Fig. 4 shows the geometrical relation between $u_{sr}^{(\ell)}$, $u_{sgr}^{(\ell)}$, and $x$-axes, where $u_{sr}^{(\ell)}$ axis points from antenna $s$ at the origin to the target at $(x_q, y_q, z_q)$, and $u_{sgr}^{(\ell)}$ axis is the projection of $u_{sr}^{(\ell)}$ axis onto the $xy$ plane. The unit vectors in $u_{sr}^{(\ell)}$, $u_{sgr}^{(\ell)}$, and $x$-axes are $\hat{u}_{sr}^{(\ell)} = [x_q^{(\ell)}, y_q^{(\ell)}, z_q^{(\ell)}]^t/R_s^{(\ell)}(0)$, $\hat{u}_{sgr}^{(\ell)} = [x_q^{(\ell)}, y_q^{(\ell)}, 0]^t/\sqrt{|x_q^{(\ell)}|^2 + |y_q^{(\ell)}|^2}$, and $\hat{x} = [1, 0, 0]^t$, respectively. The elevation angle of $u_{sr}^{(\ell)}$ axis about the $xy$ plane is $\theta_{se}^{(\ell)}$, and the azimuth angle of $u_{sgr}^{(\ell)}$ axis from $x$-axis is $\phi_{sa}^{(\ell)}$.

The $u_{sr}^{(\ell)}$, $u_{sgr}^{(\ell)}$, and $x$ coordinates of a point target are related by

$$u_{sr}^{(\ell)} = u_{sgr}^{(\ell)}\cos\theta_{se}^{(\ell)}$$

$$u_{sgr}^{(\ell)} = x \cos \phi_{sa}^{(\ell)}.$$

The spatial resolutions along these three directions are related as

$$\Delta u_{sr} = \Delta u_{sgr}^{(\ell)} \cos \theta_{se}^{(\ell)}$$
$$\Delta u_{sgr}^{(\ell)} = \Delta x^{(\ell)} \cos \phi_{sa}^{(\ell)}$$

leading to

$$\Delta x^{(\ell)} = \frac{\Delta u_{sr}}{\cos \theta_{se}^{(\ell)} \cos \phi_{sa}^{(\ell)}} = \frac{c}{2B_r \cos \theta_{se}^{(\ell)} \cos \phi_{sa}^{(\ell)}} \tag{23}$$

where the spatial resolution $\Delta u_{sr}$ is determined by the signal bandwidth and is independent of iteration. Hence, the $x$ coordinate of the $n$th range cell counted from $x_q^{(\ell)}$ is given by

$$x_s^{(\ell)}(\tau_n) = x_q^{(\ell)} + \frac{cn\Delta\tau}{2 \cos \theta_{se}^{(\ell)} \cos \phi_{sa}^{(\ell)}}$$

with $-N_r/2 \le n < N_r/2$.

Given the estimated $\alpha_{s1}^{(\ell)}$ and $\alpha_{s2}^{(\ell)}$, a compensation filter

$$H_{s\alpha}^{(\ell)}(f_\tau, \eta) = e^{j4\pi(f_c+f_\tau)(\alpha_{s1}^{(\ell)}\eta + \alpha_{s2}^{(\ell)}\eta^2)/c}$$

is multiplied with $S_{s4}^{(\ell)}(f_\tau, \eta)$ to derive

$$\begin{aligned}\tilde{S}_{s4}^{(\ell)}(f_\tau, \eta) &= S_{s4}(f_\tau, \eta) H_{s\alpha}^{(\ell)}(f_\tau, \eta) \\ &= \text{rect}\,(\eta/T_a) \sum_{n=1}^{N_q} A_{sn} \text{rect}\,(f_\tau/B_r) \\ &\quad e^{-j4\pi(f_c+f_\tau)[R_s(0)+\bar{r}_n \cdot \hat{b}_s]/c} \\ &\quad e^{-j4\pi(f_c+f_\tau)[x_n v_x + y_n(v_y - V_p)]\eta/(R_s(0)c)}\end{aligned}$$

which is inverse Fourier transformed in range to have

$$\begin{aligned}\tilde{s}_{s5}^{(\ell)}(\tau, \eta) &= \mathcal{F}_\tau^{-1}\left\{\tilde{S}_{s4}^{(\ell)}(f_\tau, \eta)\right\} \\ &\simeq \text{rect}\,(\eta/T_a) \sum_{n=1}^{N_q} A_{sn} e^{-j4\pi f_c[R_s(0)+\bar{r}_n \cdot \hat{b}_s]/c} \\ &\quad e^{-j4\pi f_c y_n (v_y - V_p)\eta/(R_s(0)c)} e^{-j4\pi f_c x_n v_x \eta/(R_s(0)c)} \\ &\quad B_r \text{sinc}\{B_r(\tau - 2([R_s(0) + \bar{r}_n \cdot \hat{b}_s]/c)\}\end{aligned} \tag{24}$$

where the second phase and the third phase terms contain information of target position $(x_n, y_n)$ and velocity $(v_x, v_y)$.

Next, design a geometrical correction filter

$$H_{sgc}^{(\ell)}(\tau, \eta) = e^{j4\pi f_c x_s^{(\ell)}(\tau) v_x^{(\ell)} \eta/(R_s^{(\ell)}(0)c)} \tag{25}$$

with $v_x^{(\ell)} = (v_{1x}^{(\ell)} + v_{2x}^{(\ell)})/2$. Multiply $H_{sgc}^{(\ell)}(\tau, \eta)$ with $\tilde{s}_{s5}^{(\ell)}(\tau, \eta)$ to have

$$\begin{aligned}\tilde{s}_{s6}^{(\ell)}(\tau, \eta) &= \tilde{s}_{s5}^{(\ell)}(\tau, \eta) H_{sgc}^{(\ell)}(\tau, \eta) = \text{rect}\,(\eta/T_a) \sum_{n=1}^{N_q} A_{sn} \\ &\quad e^{-j4\pi f_c[R_s(0)+\bar{r}_n \cdot \hat{b}_s]/c} e^{-j4\pi f_c y_n (v_y - V_p)\eta/(R_s(0)c)} \\ &\quad B_r \text{sinc}\{B_r(\tau - 2[R_s(0) + \bar{r}_n \cdot \hat{b}_s]/c)\}\end{aligned}$$

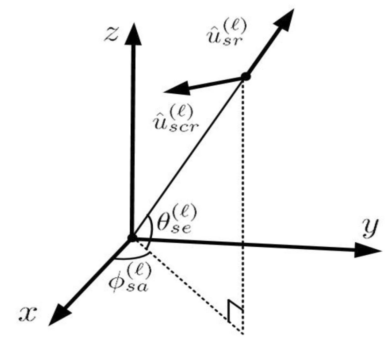


Fig. 5. Unit vectors in range and cross-range directions.

which is Fourier transformed in azimuth to have

$$\begin{aligned}\tilde{S}_{s7}^{(\ell)}(\tau, f_\eta) &= \mathcal{F}_\eta\left\{\tilde{s}_{s6}^{(\ell)}(\tau, \eta)\right\} \\ &= \sum_{n=1}^{N_q} A_n \text{rect}(f_\eta/F_a) e^{-j4\pi f_c[R_s(0)+\bar{r}_n \cdot \hat{b}_s]/c} \\ &\quad T_a \text{sinc}\left\{T_a\left(f_\eta + 2f_c(v_y - V_p)y_n/[R_s(0)c]\right)\right\} \\ &\quad B_r \text{sinc}\{B_r(\tau - 2[R_s(0) + \bar{r}_n \cdot \hat{b}_s]/c)\}\end{aligned} \tag{26}$$

where the sinc functions in $\tau$ and $f_\eta$ indicate the $n$th scatterer is located at $(\tau, f_\eta) = (\tau_n, f_{\eta n})$.

Fig. 5 shows the definitions of $\hat{u}_{sr}$ and $\hat{u}_{scr}$ in range and cross-range directions, respectively, with $u_{scr}^{(\ell)} = [\sin \phi_{sa}^{(\ell)}, -\cos \phi_{sa}^{(\ell)}, 0]^t$ and $\Delta u_{scr}^{(\ell)} = -\cos \phi_{sa}^{(\ell)} \Delta y$. A scatterer located at $(\tau_n, f_{\eta n})$ in $\tilde{S}_{s7}^{(\ell)}(\tau, f_\eta)$ is mapped to the $u_{sr}u_{scr}$ plane as

$$\begin{aligned}u_{sr}^{(\ell)} &= \frac{c}{2}\tau_n \\ u_{scr}^{(\ell)} &= \frac{\cos \phi_{sa}^{(\ell)} R_{s0}^{(\ell)} c}{2f_c(v_y^{(\ell)} - V_p)} f_{\eta n}\end{aligned} \tag{27}$$

where $v_y^{(\ell)} = (v_{1y}^{(\ell)} + v_{2y}^{(\ell)})/2$. The resolutions in the $u_{sr}u_{scr}$ plane are given by

$$\begin{aligned}\Delta u_{sr} &= \frac{c}{2}\Delta\tau \\ \Delta u_{scr}^{(\ell)} &= \frac{\cos \phi_{sa}^{(\ell)} R_{s0}^{(\ell)} c}{2f_c(v_y^{(\ell)} - V_p)} \Delta f_\eta.\end{aligned} \tag{28}$$

The parameters listed in Tables I and II imply that $\Delta u_{sr} = 25$ cm and $\Delta u_{scr} = 75$ cm.

Fig. 6 shows the image after motion compensation and geometrical correction before iteration procedure, where the target center is offset by $(\delta u_{sr}^{(\ell)}, \delta u_{scr}^{(\ell)})$ from the origin of the $u_{sr}u_{scr}$ plane, with

$$\begin{aligned}x_q^{(\ell)} &= u_{sr}^{(\ell)} \cos \phi_{sa}^{(\ell)} \cos \theta_{se}^{(\ell)} \\ z_q^{(\ell)} &= u_{sr}^{(\ell)} \sin \theta_{se}^{(\ell)}.\end{aligned}$$

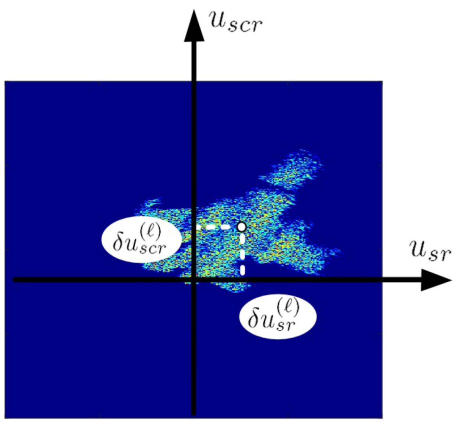


Fig. 6. Acquired ISAR image $\tilde{S}_{s7}^{(\ell)}(\tau, f_\eta)$ in $u_{sr}u_{scr}$ plane before iteration procedure ($\ell = 0$).

Since the perturbations in $\theta_{se}^{(\ell)}$ and $\phi_{sa}^{(\ell)}$ are much smaller than $\delta u_{sr}^{(\ell)}$ and $\delta u_{scr}^{(\ell)}$, we have

$$\delta x_{sq}^{(\ell)} = \delta u_{sr}^{(\ell)} \cos\phi_{sa}^{(\ell)} \cos\theta_{se}^{(\ell)} \tag{29}$$

$$\delta y_{sq}^{(\ell)} = -\frac{\delta u_{scr}^{(\ell)}}{\cos\phi_{sa}^{(\ell)}} \tag{30}$$

$$\delta z_{sq}^{(\ell)} = \delta u_{sr}^{(\ell)} \sin\theta_{se}^{(\ell)} \tag{31}$$

which are used to update the coordinates as

$$\begin{aligned} x_{sq}^{(\ell+1)} &= x_{sq}^{(\ell)} + \delta x_{sq}^{(\ell)} \\ y_{sq}^{(\ell+1)} &= y_{sq}^{(\ell)} + \delta y_{sq}^{(\ell)} \\ z_{sq}^{(\ell+1)} &= z_{sq}^{(\ell)} + \delta z_{sq}^{(\ell)}. \end{aligned} \tag{32}$$

Then, the position of the target center is updated as

$$\begin{aligned} x_q^{(\ell+1)} &= \frac{x_{1q}^{(\ell+1)} + x_{2q}^{(\ell+1)}}{2} \\ y_q^{(\ell+1)} &= \frac{y_{1q}^{(\ell+1)} + y_{2q}^{(\ell+1)}}{2} \\ z_q^{(\ell+1)} &= \frac{z_{1q}^{(\ell+1)} + z_{2q}^{(\ell+1)}}{2}. \end{aligned} \tag{33}$$

Finally, the angular direction of the target center is updated as

$$\theta_{se}^{(\ell+1)} = \tan^{-1}\frac{z_{sq}^{(\ell+1)}}{x_{sq}^{(\ell+1)}} \tag{34}$$

$$\phi_{sa}^{(\ell+1)} = \tan^{-1}\frac{y_{sq}^{(\ell+1)}}{x_{sq}^{(\ell+1)}}. \tag{35}$$

The iteration procedure is summarized as follows.

*Step 1:* Set $\ell = 0$, estimate the initial target position with (7)–(10).

*Step 2:* Estimate coefficients $\beta_{s1}^{(\ell)}$, $\beta_{s2}^{(\ell)}$, and $\beta_{s3}^{(\ell)}$ embedded in (11).

*Step 3:* Estimate coefficients $\alpha_{s1}^{(\ell)}$ and $\alpha_{s2}^{(\ell)}$ with the RFRT-FrFT algorithm in Section IV-A.

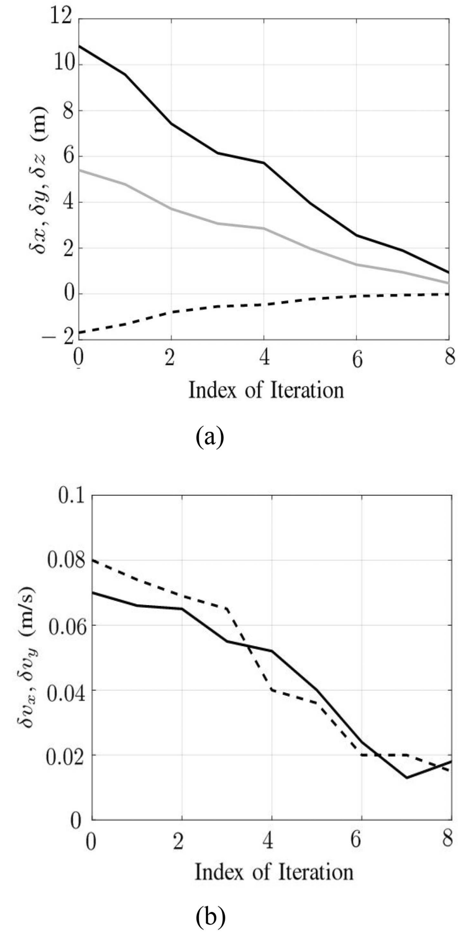


Fig. 7. Estimation errors with iterations. (a) Position errors, ———: $\delta x$, – – –: $\delta y$ and ———: $\delta z$. (b) Velocity errors, ———: $\delta v_x$ and – – –: $\delta v_y$.

*Step 4:* Estimate the target velocity $v_{sx}^{(\ell)}$ and $v_{sy}^{(\ell)}$ with (21) and (22).

*Step 5:* Acquire ISAR image with the geometrical correction filter in (25) and map it to the $u_{sr}u_{scr}$ plane with (27).

*Step 6:* Compute the position deviation with (29)–(31), then update the target position with (32) and (33).

*Step 7:* Update the target angular direction with (34) and (35).

*Step 8:* Set $\ell \leftarrow \ell + 1$, then go to Step 2. The iteration is halted if $|R_{s0}^{(\ell+1)} - R_{s0}^{(\ell)}| < \Delta u_{sr}$.

Fig. 7 shows that the estimation errors of position and velocity, respectively, of the target diminish with iterations. The acquired image also becomes more focused as the iteration moves on.

## V. Image Quality and Target Recognition

Fig. 8 shows the orientations of $\zeta_h, \zeta_v, u_{sr}$, and $u_{sgr}$ in the $xyz$ coordinates. The $\zeta_h\zeta_v$ plane is orthogonal to the $u_{sr}$ direction, and $\zeta_h$ is parallel to the $xy$ plane. Coordinates $(\zeta_h, \zeta_v)$ are related to coordinates $(u_{sr}, u_{scr})$ as

$$\begin{aligned} \zeta_v \cos\theta_{se} &= \sin\theta_{se} u_{sr} \\ \zeta_h &= u_{scr} \end{aligned}$$

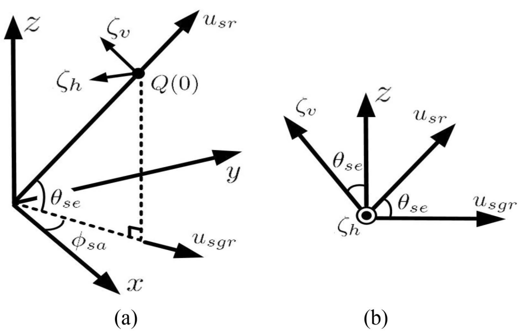


Fig. 8. Orientations of $\zeta_h$, $\zeta_v$, $u_{sr}$, and $u_{sgr}$ (a) in $xyz$ coordinates, (b) on $u_{sgr}z$ plane.

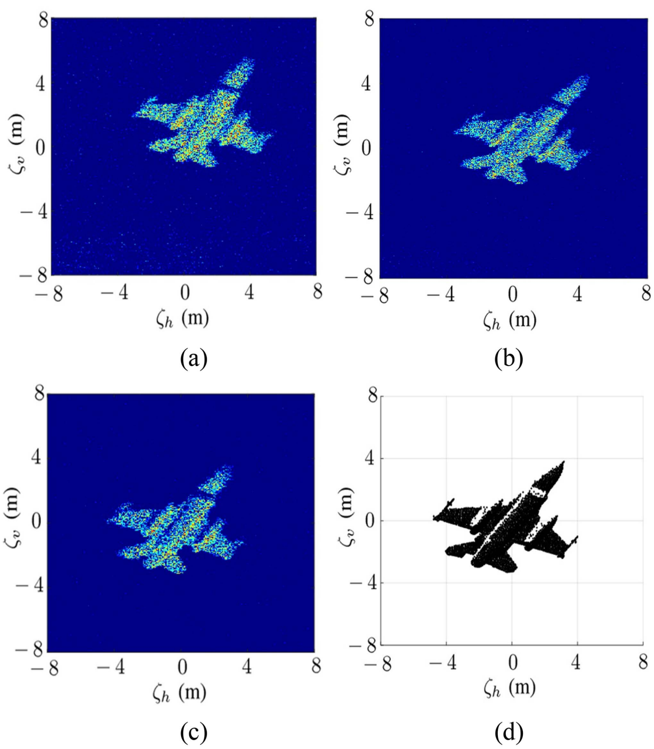


Fig. 9. ISAR images (in dB) of an F-16 Fighting Falcon acquired with the proposed approach after iteration $\ell$,. (a) $\ell = 0$. (b) $\ell = 4$. (c) $\ell = 8$. (d) Scan image of a 3-D model.

and the resolutions in the $\zeta_h\zeta_v$ plane are

$$\Delta\zeta_v = \tan\theta_{se}\Delta u_{sr}$$
$$\Delta\zeta_h = \Delta u_{scr}.$$

An acquired ISAR image mapped to the $\zeta_h\zeta_v$ plane resembles a visual-like image viewed from the origin.

Fig. 9(a)–(c) shows the ISAR images of an F-16 Fighting Falcon acquired with the proposed iteration procedure summarized at the end of Section IV. At $\ell = 0$, the target center deviates from the image center because the initial target direction is not accurately estimated. Such deviation affects not only the estimation of target motion parameters but also the reconstructed target shape and features. As the iteration moves on, the target center gradually shifts to the image center. After iteration $\ell = 8$, the target shape and features become more similar to the scan image of the true target shown in Fig. 9(d).

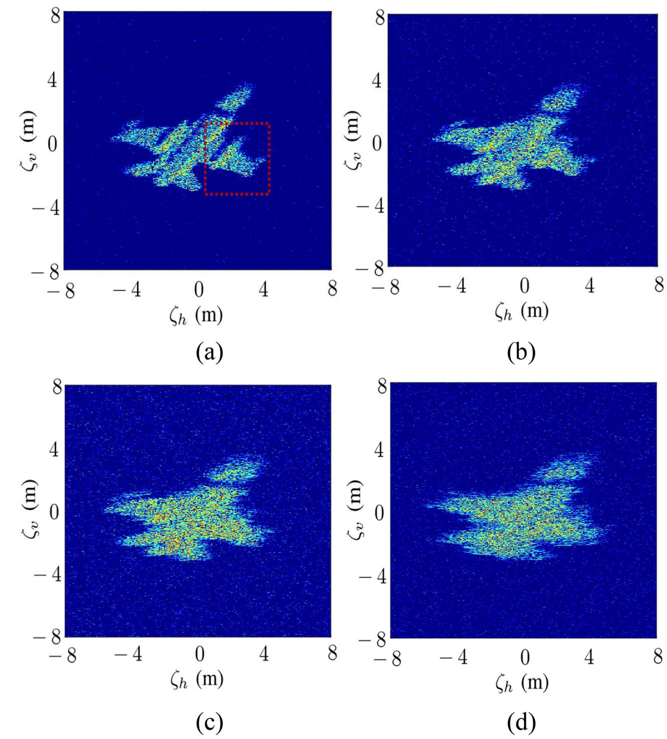


Fig. 10. Acquired ISAR images (in dB) of an F-16 Fighting Falcon, SNR = 5 dB. (a) Proposed approach, $\mathcal{E} = 4.54$. (b) Method in [30], $\mathcal{E} = 4.75$. (c) PGA in [29], $\mathcal{E} = 4.81$. (d) Proposed approach but without compensating attitude perturbation, $\mathcal{E} = 4.92$.

Equation (25) indicates that error in the target velocity component $v_x$ contributes additional Doppler shift in the range direction. Equation (27) indicates that the correct target velocity component $v_y$ is needed to map the azimuth-frequency coordinate to the cross-range coordinate. In this work, an iteration procedure is developed and summarized at the end of Section IV to estimate accurate target position and acquire a more faithful ISAR image. The simulations are run with MATLAB R2019a on a PC with i7-3.00 GHz CPU and 32 GB memory. It takes 83 CPU s to conduct one iteration.

### A. Comparison With Other Techniques

Nonparameteric approach, such as phase gradient algorithm (PGA), has been widely used to compensate the phase error embedded in a SAR or ISAR image [29]. FrFT method has also been used to estimate the phase error induced by target motion [30]. For a high-speed aerial target, the range-compressed signals spread across many range cells, increasing the computational time for estimating the phase error terms and decreasing the estimation accuracy, especially at low SNR. In this work, RFRT is applied first to concentrate the signals to a small number of range cells, followed by FrFT to estimate the motion parameters.

Fig. 10 shows the acquired ISAR images of an F-16 Fighting Falcon with different approaches. The partial images within a dash-square marked in Fig. 10(a) are magnified and shown in Fig. 11. Both Figs. 10(a) and 11(a) show clear images after

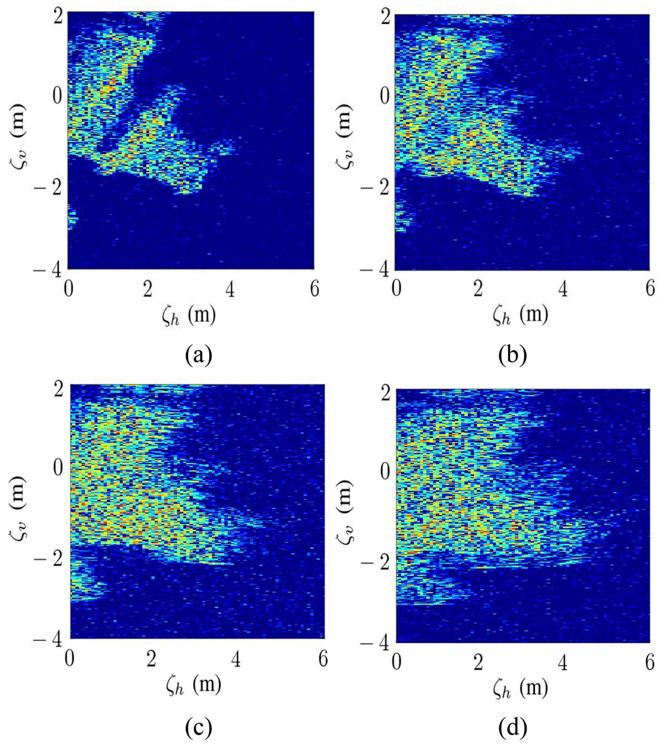

Fig. 11. Zoom-in of dashed-square area in Fig. 10 (in dB) of an F-16 Fighting Falcon, SNR = 5 dB, (a) proposed approach, (b) method in [30], (c) PGA in [29], (d) proposed approach but without compensating attitude perturbation. Parameters are the same as in Fig. 10.

TABLE IV
COMPARISON OF CPU TIME

| method | CPU time |
|---|---|
| proposed approach | 657 s |
| method in [30] | 597 s |
| PGA in [29] | 768 s |
| proposed approach w/o compensating attitude perturbation | 642 s |

applying the proposed approach to compensate the errors caused by target motion and attitude perturbation of platform. Fig. 10(b) and (c) shows the smeared images because the phase errors are not completely removed. Fig. 10(d) shows that the phase difference aroused by attitude perturbation of the platform can seriously blur the image.

The required CPU times to run eight iterations with the methods referred to in Fig. 10 are listed in Table IV.

Entropy of an image is often used to evaluate its clearness [31] or concentration of energy among pixels [9]. In this work, the entropy of an image is computed as [9]

$$\mathcal{E} = \sum_{n=1}^{N_x}\sum_{m=1}^{N_y} \frac{I_{nm}^2}{I_{\rm tot}} \ln \frac{I_{\rm tot}}{I_{nm}^2}$$

where $N_x$ and $N_y$ are the numbers of pixels in $x$ and $y$ directions, respectively,

$$I_{nm} = 20\log_{10}|\tilde{S}_{s7}(\tau, f_\eta)|$$

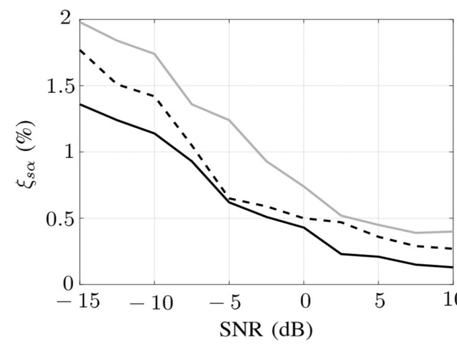


Fig. 12. Range estimation error $\xi_\alpha$ versus SNR. ———: proposed approach. – – –: [30]. ———: PGA [29].

is the intensity (in dB) at the $nm$th pixel, and

$$I_{\rm tot} = \sum_{n=1}^{N_x}\sum_{m=1}^{N_y} I_{nm}^2$$

is the square-sum of pixel intensities.

To characterize the noise level in the backscattered signals, an SNR is defined as [30], [32]

$$\text{SNR} = 10\log_{10}\frac{P_{\rm avg}}{P_n}$$

where $P_{\rm avg}$ is the average power of the backscattered signal $s_{s1}(\tau, \eta)$ and $P_n$ is the power of white Gaussian noise.

Let us define a range estimation error as

$$\xi_{s\alpha} = 100 \times \frac{\int_{-T_a/2}^{T_a/2}|\Delta\tilde{R}_{st}(\eta) - \Delta R_{st}(\eta)|d\eta}{\int_{-T_a/2}^{T_a/2}|\Delta R_{st}(\eta)|d\eta} \ (\%).$$

Fig. 12 shows the range estimation error $\xi_{s\alpha}$ versus SNR associated with the ISAR images of the F-16 Fighting Falcon. A smaller error of the proposed approach is attributed to the RFRT-FrFT method for yielding more accurate estimation on the $\alpha$ coefficients, especially at low SNR.

## *B. Target Recognition*

Four different high-speed aerial targets are simulated for ISAR imaging, including F-16 Fighting Falcon, F-35 Lightning, J-10 Mighty Dragon, and Dassault Rafale. The surface of these fighter planes are approximated as PEC [17], and the backscattered signals are simulated by applying the PO method on these surfaces [16], ignoring edge diffraction, and absorbing coating.

Fig. 13 shows the ISAR images of these four fighter planes in the $\zeta_h\zeta_v$ plane acquired with the proposed approach. The geometrical features of each aerial target are well discernible for identification.

Fig. 14 shows the cumulative distribution function (CDF) of pixel intensity in the acquired SAR images of the four fighter planes. The backscattering radar cross section of F-35 is much lower than the other three, due to its stealth geometry. Note that the absorbing coating is not considered in the simulations.

To enable automatic recognition, the contour of targets shown in Fig. 13 are first extracted by applying edge detection filters $h_h$ and $h_v$ for horizontal and vertical edges, respectively, with

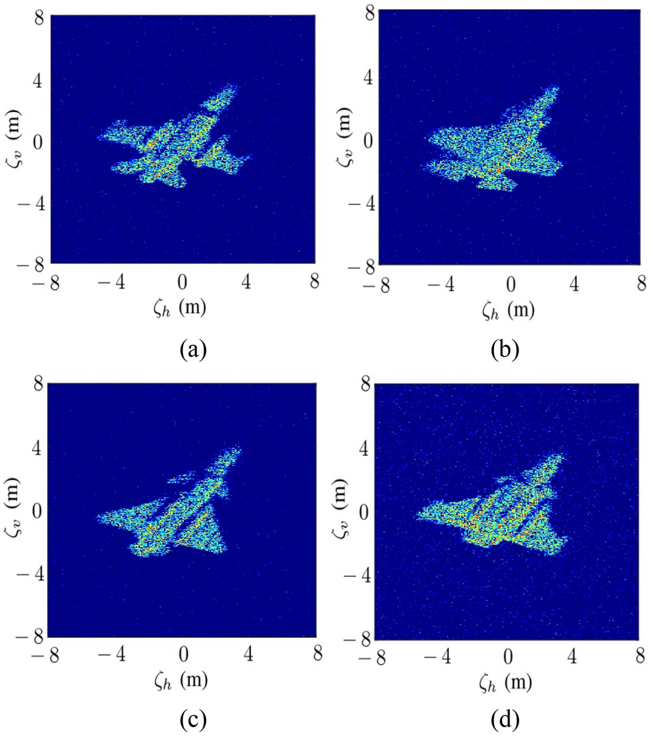


Fig. 13. Acquired ISAR images (in dB) in $\zeta_h\zeta_v$ plane, SNR $= 5$ dB. (a) F-16 Fighting Falcon. (b) F-35 Lightning. (c) J-10 Mighty Dragon. (d) Dassault Rafale.

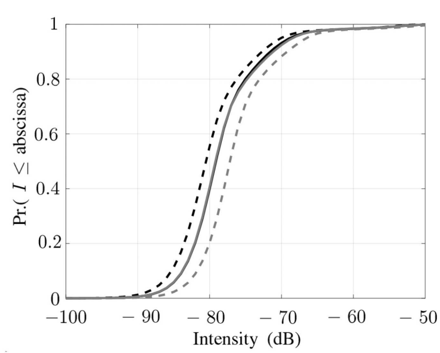


Fig. 14. CDF of pixel intensity in the acquired SAR images. ———: F-16. — — —: F-35. ———: J-10. — — —: Rafale.

the explicit forms [33]

$$h_h = \begin{bmatrix} 1 & 1 & 1 \\ 0 & 0 & 0 \\ -1 & -1 & -1 \end{bmatrix}, \quad h_v = \begin{bmatrix} -1 & 0 & 1 \\ -1 & 0 & 1 \\ -1 & 0 & 1 \end{bmatrix}.$$

By taking 2-D convolution of these two filters with image intensity $I_{nm}$, the horizontal edges are detected from

$$I_{h,nm} = I_{n(m+1)} - I_{n(m-1)}$$

and the vertical edges are detected from

$$I_{v,nm} = I_{(n+1)m} - I_{(n-1)m}.$$

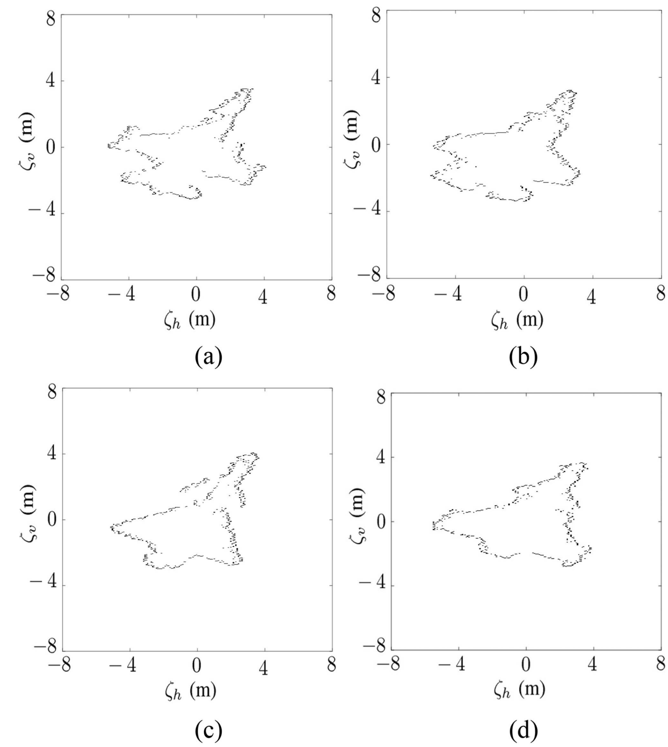


Fig. 15. Contour of fighter planes, SNR $= 5$ dB. (a) F-16 Fighting Falcon. (b) F-35 Lightning. (c) J-10 Mighty Dragon. (d) Dassault Rafale.

The intensity for edge detection is given by [33]

$$I_{vh,nm} = \sqrt{I_{h,nm}^2 + I_{v,nm}^2}.$$

Fig. 15 shows the contours of fighter planes presented in Fig. 13. Salient geometrical features of each fighter plane are manifested, including fuselage, wing, and canard, which are useful for identification. The image and contour of each fighter plane is pending on the relative position between target and platform, as well as the target attitude.

Fig. 16 shows the acquired images at SNR $= -10$ dB, which are smudged by noises and look fuzzier than their counterparts in Fig. 13. Fig. 17 shows the contours of fighter planes extracted from the images in Fig. 16.

At SNR $= 5$ dB, the ISAR images in Fig. 13 are clear and free of speckles, hence the contours of these four fighters are definitely drawn, as shown in Fig. 15. At SNR $= -10$ dB, the noise tends to jitter the boundary between target and background in the image, as shown in Fig. 16. Moreover, more speckles appear in the background around the target, making it more difficult to draw the contour of a target, as shown in Fig. 17.

Next, a geometrical matching method is proposed to recognize different types of fighter. The center of each target is first determined from the contours shown in Fig. 15. Let $r_g(\phi)$ be the distance between the center and a point on the contour with perimeter angle $\phi$, where $g$ stands for the $g$th target, and $\phi \in (-\pi, \pi]$. The range difference between the $g$th and the $q$th targets at $\phi$ is

$$\Delta R_{gq}(\phi) = r_g(\phi) - r_q(\phi).$$

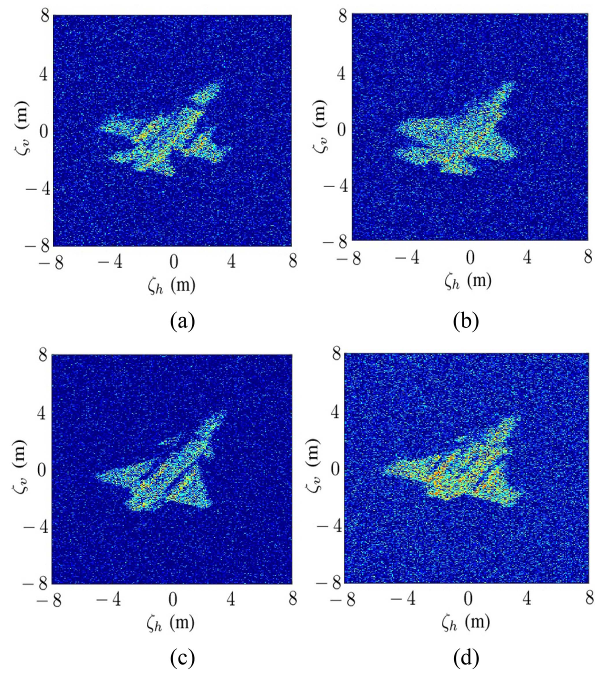


Fig. 16. Acquired ISAR images (in dB) in $\zeta_h \zeta_v$ plane, SNR $= -10$ dB. (a) F-16 Fighting Falcon. (b) F-35 Lightning. (c) J-10 Mighty Dragon. (d) Dassault Rafale.

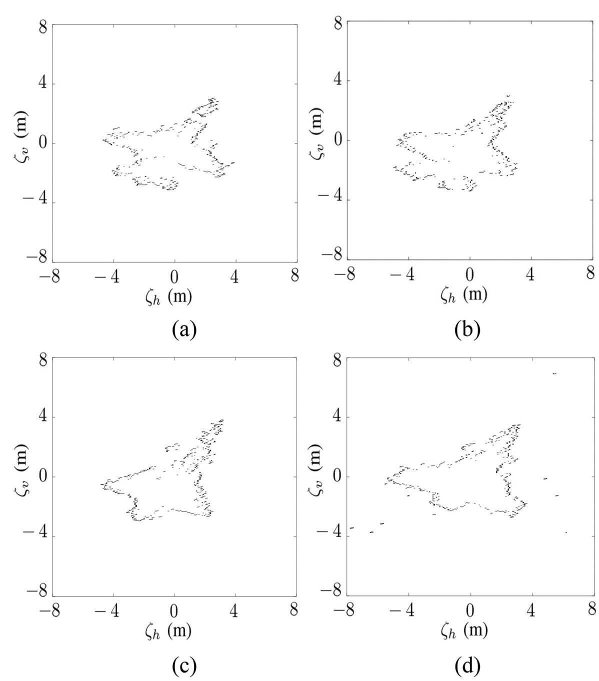


Fig. 17. Contour of fighter planes, SNR $= -10$ dB. (a) F-16 Fighting Falcon. (b) F-35 Lightning. (c) J-10 Mighty Dragon. (d) Dassault Rafale.

Then, a matching factor between these two targets is defined as

$$\mathcal{M}_{gq} = \sqrt{\frac{1}{N_\phi} \sum_{\phi=0}^{N_\phi - 1} [\Delta R_{gq}(\phi)]^2}$$

where $N_\phi$ is the sample number of $\phi$'s along the whole perimeter.

TABLE V
MATCHING FACTOR $\mathcal{M}_{gq}$: (A) SNR $= 5$ DB AND (B) SNR $= -10$ DB

| (a) | F-16 | F-35 | J-10 | Rafale |
|---|---|---|---|---|
| F-16 | 0 m | 3.09 m | 2.48 m | 2.45 m |
| F-35 | 3.09 m | 0 m | 2.40 m | 2.89 m |
| J-10 | 2.48 m | 2.40 m | 0 m | 2.66 m |
| Rafale | 2.45 m | 2.89 m | 2.66 m | 0 m |

| (b) | F-16 | F-35 | J-10 | Rafale |
|---|---|---|---|---|
| F-16 | 0 m | 3.39 m | 2.94 m | 12.99 m |
| F-35 | 3.39 m | 0 m | 2.03 m | 13.01 m |
| J-10 | 2.94 m | 2.03 m | 0 m | 13.05 m |
| Rafale | 12.99 m | 13.01 m | 13.05 m | 0 m |

Table V lists the matching factors between all possible pairs among the four fighters, with SNR $= 5$ and $-10$ dB, respectively. The matching factors are effective for recognizing different fighter planes, even when the acquired images become blurred.

### C. Highlight of Contributions

The contributions of this work are highlighted as follows.

1) A novel ISAR imaging approach, based on a moving vessel bearing attitude perturbation, is proposed to acquire high-resolution ISAR image of high-speed aerial targets within a short aperture time.
2) A $(\zeta_h, \zeta_v)$ plane is proposed to display ISAR images in visual-like format, which can be upgraded to holograph-like images.
3) An iteration procedure is developed to fine-tune the target velocity $(v_x, v_y)$ and target position $(x_q, y_q, z_q)$ more accurately.
4) Geometrical distortion is compensated with accurate $v_x$, and correct cross-range scaling is achieved with accurate $v_y$.
5) PO method is used to simulate the backscattered signals from different aerial targets in various attitudes and relative positions. The radar parameters can be flexibly adjusted to prove the concept of various potential applications of ISAR imaging.

## VI. CONCLUSION

An ISAR imaging approach on high-speed aerial targets, with radar installed on a moving vessel, has been developed and verified by simulations. The range difference caused by platform perturbation is compensated by using the attitude data of the vessel. The backscattered signals are simulated with a PO method. The motion parameters of the target are estimated with an RFRT-FrFT approach. An iteration procedure has been developed to achieve more accurate target velocity and target position, as well as acquire more faithful target image. A $(\zeta_h, \zeta_v)$ plane is proposed to display ISAR images in visual-like format, which can be upgraded to holograph-like images. The acquired images are well recognizable among four similar fighter planes by simulations, even at low SNR.

## References


[1] V. C. Chen and M. Martorella, *Inverse Synthetic Aperture Radar Imaging: Principles, Algorithms and Applications*. Edison, NJ, USA: Inst. Eng. Technol., 2014.

[2] S. Zhang, Y. Liu, X. Li, and G. Bi, "Joint sparse aperture ISAR autofocusing and scaling via modified newton method-based variational Bayesian inference," *IEEE Trans. Geosci. Remote Sens.*, vol. 57, no. 7, pp. 4857–4869, Jul. 2019.

[3] M. Wang, S. Yang, Z. Liu, and Z. Li, "Collaborative compressive radar imaging with saliency priors," *IEEE Trans. Geosci. Remote Sens.*, vol. 57, no. 3, pp. 1245–1255, Mar. 2019.

[4] Y. Wang and X. Chen, "3-D interferometric inverse synthetic aperture radar imaging of ship target with complex motion," *IEEE Trans. Geosci. Remote Sens.*, vol. 56, no. 7, pp. 3693–3708, Jul. 2018.

[5] L. Liu, F. Zhou, X. Bai, J. Paisley, and H. Ji, "A modified EM algorithm for ISAR scatterer trajectory matrix completion," *IEEE Trans. Geosci. Remote Sens.*, vol. 56, no. 7, pp. 3953–3962, Jul. 2018.

[6] Y. Zhou, L. Zhang, and Y. Cao, "Dynamic estimation of spin spacecraft based on multiple-station ISAR images," *IEEE Trans. Geosci. Remote Sens.*, vol. 58, no. 4, pp. 2977–2989, Apr. 2020.

[7] Y. Zhou, L. Zhang, and Y. Cao, "Attitude estimation for space targets by exploiting the quadratic phase coefficients of inverse synthetic aperture radar imagery," *IEEE Trans. Geosci. Remote Sens.*, vol. 57, no. 6, pp. 3858–3872, Jun. 2019.

[8] F. Berizzi, E. D. Mese, M. Diani, and M. Martorella, "High-resolution ISAR imaging of maneuvering targets by means of the range instantaneous Doppler technique: Modeling and performance analysis," *IEEE Trans. Image Process.*, vol. 10, no. 12, pp. 1880–1890, Dec. 2001.

[9] J. Wang, L. Zhang, L. Du, D. Yang, and B. Chen, "Noise-robust motion compensation for aerial maneuvering target ISAR imaging by parametric minimum entropy optimization," *IEEE Trans. Geosci. Remote Sens.*, vol. 57, no. 7, pp. 4202–4217, Jul. 2019.

[10] Y. Du, Y. Jiang, Y. Wang, W. Zhou, and Z. Liu, "ISAR imaging for low-earth-orbit target based on coherent integrated smoothed generalized cubic phase function," *IEEE Trans. Geosci. Remote Sens.*, vol. 58, no. 2, pp. 1205–1220, Feb. 2020.

[11] Y. Wang, X. Huang, and R. Cao, "Novel approach for ISAR cross-range scaling based on the multidelay discrete polynomial-phase transform combined with keystone transform," *IEEE Trans. Geosci. Remote Sens.*, vol. 58, no. 2, pp. 1221–1231, Feb. 2020.

[12] B. Kang, B. Ryu, and K. Kim, "Bistatic ISAR imaging for nonuniformly rotating targets," *IEEE Trans. Aerosp. Electron. Syst.*, vol. 55, no. 4, pp. 1972–1988, Aug. 2019.

[13] D. Li, J. Ren, H. Liu, Z. Yang, J. Wan, and Z. Chen, "A novel ISAR imaging approach for maneuvering targets with satellite-borne platform," *IEEE Geosci. Remote Sens. Lett.*, vol. 19, Aug. 26, 2021, Art no. 4017105.

[14] H. Shi, S. Xia, Q. Qin, T. Yang, and Z. Qiao, "Non-stationary platform inverse synthetic aperture radar maneuvering target imaging based on phase retrieval," *Sensors*, vol. 18, no. 10, May 2018, Art. no. 3333.

[15] V. Backstrom and A. Skarbratt, "Maritime ISAR imaging with airborne radar," Master Thesis, Dept. of Radio and Space science, Chalmers University of Technology, Goteborg, Sweden, 2010.

[16] J. Cai, M. Martorella, Q. Liu, Z. Ding, E. Giusti, and T. Long, "Automatic target recognition based on alignments of three-dimensional interferometric ISAR images and CAD models," *IEEE Trans. Aerosp. Electron. Syst.*, vol. 56, no. 6, pp. 4872–4888, Dec. 2020.

[17] J. I. Lee and D. W. Seo, "Fast scattered far-field predictions for super-resolution ISAR image formation using the shooting and bouncing ray technique," *IEEE Access*, vol. 10, pp. 18182–18191, 2022.

[18] L. Liu, F. Zhou, X. Bai, M. Tao, and Z. Zhang, "Joint cross-range scaling and 3D geometry reconstruction of ISAR targets based on factorization method," *IEEE Trans. Image Process.*, vol. 25, no. 4, pp. 1740–1750, Apr. 2016.

[19] A. Kumar, E. Giusti, F. Mancuso, S. Ghio, A. Lupidi, and M. Martorella, "Three-dimensional polarimetric InISAR imaging of non-cooperative targets," *IEEE Trans. Comput. Imag.*, vol. 9, pp. 210–223, Feb. 2023.

[20] Y. Wang, J. Rong, and T. Han, "Novel approach for high resolution ISAR/InISAR sensors imaging of maneuvering target based on peak extraction technique," *IEEE Sensors J.*, vol. 19, no. 14, pp. 5541–5558, Jul. 2019.

[21] J. Rong, Y. Wang, and T. Han, "Interferometric ISAR imaging of maneuvering targets with arbitrary three-antenna configuration," *IEEE Trans. Geosci. Remote Sens.*, vol. 58, no. 2, pp. 1102–1119, Feb. 2020.

[22] Q. Lv and S. Zhang, "Three-dimensional interferometric ISAR imaging algorithm based on cross coherence processing," *Sensors*, vol. 21, no. 15, 2021, Art. no. 5073.

[23] B. Zhou, X. Qi, J. Zhang, and H. Zhang, "Effect of 6-DOF oscillation of ship target on SAR imaging," *Remote Sens.*, vol. 13, no. 9, May 2021, Art. no. 1821.

[24] S. Shao, L. Zhang, and H. Liu, "High-resolution ISAR imaging and motion compensation with 2-D joint sparse reconstruction," *IEEE Trans. Geosci. Remote Sens.*, vol. 58, no. 10, pp. 6791–6811, Oct. 2020.

[25] X. Tan et al., "An efficient range-Doppler domain ISAR imaging approach for rapidly spinning targets," *IEEE Trans. Geosci. Remote Sens.*, vol. 58, no. 4, pp. 2670–2681, Apr. 2020.

[26] S. Zhang, Y. Liu, and X. Li, "Computationally efficient sparse aperture ISAR autofocusing and imaging based on fast ADMM," *IEEE Trans. Geosci. Remote Sens.*, vol. 58, no. 12, pp. 8751–8765, Dec. 2020.

[27] Z. Cao, P. Chen, Z. Chen, and Y. Jin, "DOA estimation for multiple targets in MIMO radar with nonorthogonal signals," *Math. Problems Eng.*, 2018, Art. no. 6465856.

[28] P. Huang, X. Xia, Y. Gao, X. Liu, G. Liao, and X. Jiang, "Ground moving target refocusing in SAR imagery based on RFRT-FrFt," *IEEE Trans. Geosci. Remote Sens.*, vol. 57, no. 8, pp. 5476–5492, Aug. 2019.

[29] D. E. Wahl, P. H. Eichel, D. C. Ghiglia, and C. V. Jakowatz, "Phase gradient autofocus-a robust tool for high resolution SAR phase correction," *IEEE Trans. Aerosp. Electron. Syst.*, vol. 30, no. 3, pp. 827–835, Jul. 1994.

[30] Z. Ding et al., "A ship ISAR imaging algorithm based on generalized radon-fourier transform with low SNR," *IEEE Trans. Geosci. Remote Sens.*, vol. 57, no. 9, pp. 6385–6396, Sep. 2019.

[31] Z. Yang, D. Li, X. Tan, H. Liu, L. Xu, and G. Liao, "An efficient ISAR imaging approach for highly maneuvering targets based on subarray averaging and image entropy," *IEEE Trans. Geosci. Remote Sens.*, vol. 60, Jul. 2021, Art no. 5102113.

[32] H. Fan, L. Ren, E. Mao, and Q. Liu, "A high-precision method of phase-derived velocity measurement and its application in motion compensation of ISAR imaging," *IEEE Trans. Geosci. Remote Sens.*, vol. 56, no. 1, pp. 60–77, Jan. 2018.

[33] S. Mehrotra, S. Das, S. Shikha, and C. Kar, "Comparative analysis of traditional methods with game of life in cellular automata for edge detection," *Int. J. Comput. Appl.*, vol. 118, no. 18, pp. 18–24, May 2015.


**Dau-Ming Wu** was born in Kaohsiung City, Taiwan, on 11 September, 1995. He received the B.S. degree in electronic engineering from the Department of Electronic Engineering, National Changhua University of Education, Changhua, Taiwan, in 2018, and the M.S. degree in electronic engineering from the Graduate Institute of Communication Engineering, National Taiwan University, Taipei, Taiwan, in 2022.

Since August 2022, he has been an Antenna Engineer with Tron Future Technology, Hsinchu, Taiwan. His research interests include radar signal processing, synthetic aperture radar, digital image process, and antenna and electromagnetic circuit design.

**Jean-Fu Kiang** (Life Senior Member, IEEE) received the Ph.D. degree in electrical engineering from the Massachusetts Institute of Technology, Cambridge, MA, USA, in 1989.

Since 1999, he has been a Professor with the Department of Electrical Engineering and the Graduate Institute of Communication Engineering, National Taiwan University, Taipei, Taiwan. His research focuses to explore different ideas, theories, and methods on various electromagnetic phenomena and possible applications, including remote sensing, radar signal processing, antennas, phased arrays, propagation, scattering, communications, and so on.